

A high-fidelity quantum matter-link between ion-trap microchip modules

M. Akhtar^{1,2,†}, F. Bonus^{2,3,†}, F. R. Lebrun-Gallagher^{1,2,†}, N. I. Johnson¹, M. Siegele-Brown¹, S. Hong¹, S. J. Hile¹, S. A. Kulmiya⁴, S. Weidt^{1,2} and W. K. Hensinger^{1,2,*}

¹*Sussex Centre for Quantum Technologies, University of Sussex, Brighton, BN1 9RH, UK*

²*Universal Quantum Ltd, Brighton, BN1 6SB, UK*

⁴*Department of Physics and Astronomy, University College London, London, WC1E 6BT, UK*

³*Quantum Engineering Centre for Doctoral Training, University of Bristol, Bristol, BS8 1TH, UK*

(Dated: 29th March 2022)

System scalability is fundamental for large-scale quantum computers (QCs) and is being pursued over a variety of hardware platforms [1–6]. For QCs based on trapped ions, architectures such as the quantum charge-coupled device (QCCD) are used to scale the number of qubits on a single device [7, 8]. However, the number of ions that can be hosted on a single quantum computing module is limited by the size of the chip being used. Therefore, a modular approach is of critical importance and requires quantum connections between individual modules. Here, we present the demonstration of a quantum matter-link in which ion qubits are transferred between adjacent QC modules. Ion transport between adjacent modules is realised at a rate of 2424 s^{-1} and with an ion-transfer fidelity in excess of 99.99993%. Furthermore, we show that the link does not measurably impact the phase coherence of the qubit. The realisation of the quantum matter-link demonstrates a novel mechanism for interconnecting QCCD devices. This achieves a key milestone for the implementation of modular QCs capable of hosting millions of trapped-ion qubits.

Keywords: quantum information, scalable quantum computation, ion trapping, atomic and molecular physics

I. INTRODUCTION

Platforms using trapped atomic ions form an exceptional foundation on which QCs and quantum simulators can be developed [9]. Encoding qubits in the internal electronic states of trapped ions offers the highest quantum gate fidelities and the longest coherence times when compared to other QC architectures [10–15].

So far, small-scale trapped-ion QCs with up to 10s of qubits have been realised [16–19]. Generally, a single trapping region is used to confine a linear crystal of trapped ions acting as a qubit register. Quantum logic using multiple qubits is achieved through the Coulomb interaction within the crystal. However, limits on the motional mode density make it challenging to scale a single register to larger qubit numbers [20].

One architecture that allows for multiple qubit registers in its design is the quantum charged-couple device (QCCD) which consists of an array of segmented electrodes [7, 8]. Locations or zones within a single device can be allocated specific functions, such as quantum information processing, memory and read-out. This configuration allows for small qubit registers to be interfaced to one another via mobile ions. Experimental work has shown that the transport of ion qubits within a single device can be realised with high-fidelity and without loss of coherence [21]. Furthermore, the QCCD architecture has the potential to be paired with laser-free gate schemes to implement high-fidelity universal quantum logic [12, 22].

Recently, QCCD architectures have been used to demonstrate fault-tolerant quantum computation [18, 23, 24].

To unlock many of the anticipated applications of a QC within the necessary level of error correction, far larger qubit numbers will be required than are available on current devices [25–27]. For example, simulations of the FeMoco molecule could lead to a better understanding of nitrogen fixation for the production of ammonia in fertilisers, but simulating its ground state would require many millions of qubits [26]. Incorporating these large numbers of qubits into a single QCCD does not appear feasible given the size limitations of a single device. A realistic ion-trap QC architecture must therefore be constructed from a network of QC modules and offer inter-module connection rates that are orders of magnitude faster than qubit decoherence times.

Thus far, the only experimentally demonstrated method used to connect trapped-ion QC modules relies on photonic links [1, 4, 28, 29]. This optical interface permits the heralded, probabilistic distribution of entanglement between remote modules. Figure 1a briefly describes the processes involved in implementing a photonic link for an ion-trap QC. Photonic interconnects between two QC modules have been realised with an entanglement connection rate of 182 s^{-1} at an entanglement fidelity of 94% [4]. Large optical switch arrays and wavelength conversion schemes offer a pathway towards connecting multiple modules together for large scale QCs. However, implementing these solutions in a fault-tolerant QC, would currently achieve an effective connection rate that is ~ 2 orders of magnitude less than the raw entanglement rate (see Methods). This reduces the rate to a level that is comparable to the qubit decoherence time ($\sim 1\text{ s}$) [9]. While techniques to improve photon collection efficiencies

[†] These authors contributed equally to this work.

* w.k.hensinger@sussex.ac.uk

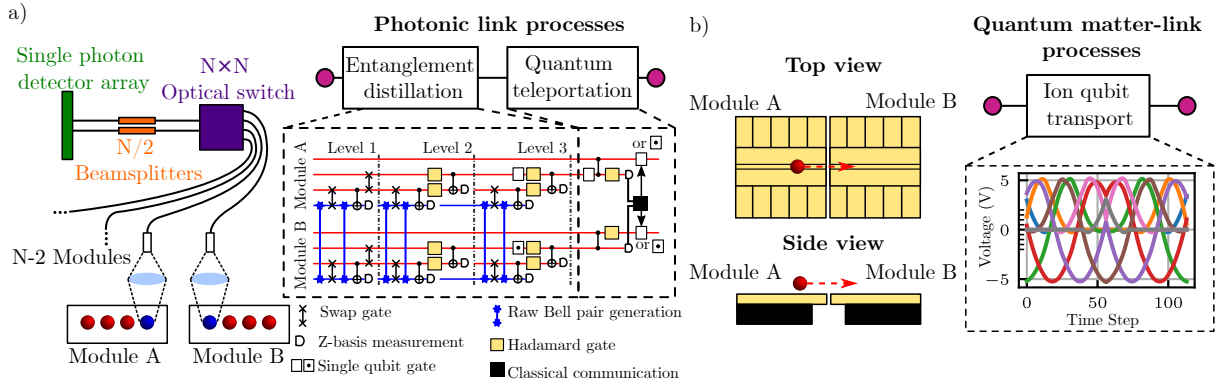


Figure 1. An illustration of the process for connecting two modules (Module A and Module B) for the purposes of a modular ion-trap QC. a) Photonic links use probabilistic, heralded entanglement which is generated from the interference of emitted photons from each module. The red and blue spheres denote different ion species. An $N \times N$ optical switch links the modules, where N is the number of modules. The emitted photons interfere at the beam splitter and a single photon detector array is used to herald the generation of entanglement between modules. In order to generate a high-fidelity link between modules a distillation process is required. The dashed box represents a proposal for a 3 level distillation process that would take a 94% entanglement fidelity to 99.7% fidelity, more details can be found in Ref.[30]. After distillation, quantum teleportation can then be used to map the qubit state between modules, thereby completing the information transfer. b) Linking modules using ion qubit transport. DC voltage waveforms control the ion motion such that the ion qubit is physically transported between the modules. The dashed box contains a plot of the voltage shuttling waveforms used in this work, each plot colour denotes a different DC electrode. Here the modules are depicted as surface traps but other geometries are also applicable. This method does not require quantum gates. Furthermore, for a QC architecture based on quantum matter-links, multi-species gates are not necessary.

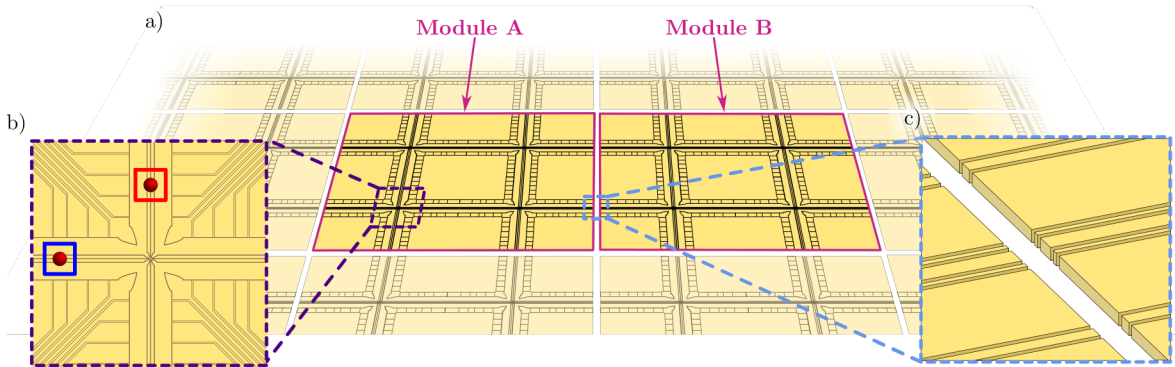


Figure 2. An illustration of a small section of a modular version of the QCCD quantum computer architecture. a) Two modules (“Module A” and “Module B”) are shown as fully opaque and parts of ten other modules are shown as partially transparent. As an example, each module contains 4 X-junctions and is structured such that it tessellates with neighbouring modules. Inset b) shows a single X-junction on a module. For this architecture, specific areas of the X-junction are associated with certain functions. For instance, a qubit may be located in a gate zone for quantum logic operations (blue box) while another qubit may be stored in a memory zone (red box). Inset c) depicts the gap separating the modules. The electrodes that create a confining potential for the ions extend out to the edge of the module such that ions can be moved to the neighbouring module.

such as on-chip cavities could increase the entanglement rate, their integration within ion-trap modules remains an unsolved and difficult challenge [31].

Lekitsch et al. proposed an alternative approach to scaling trapped-ion QCs where ion qubit transfer is mediated by electric fields [22]. Figure 1b highlights the processes involved in using a quantum matter-link for an ion-trap QC. In the illustration, surface-electrode ion-trap modules are depicted with an electrode structure that spans to the module’s edge. When the electrodes

on the edge of each module are aligned with respect to its neighbour, ions can be moved with translating potentials from one module, across the inter-module gap, to the next [22]. Figure 2 shows an example of how this method might be implemented on a large scale. It illustrates a conceptual modular QCCD architecture within which quantum information is distributed using inter-module ion qubit transport. Using this architecture, it is then possible to build a quantum network of tessellated QC modules. A first step towards realising inter-module

transport was made by Stopp et al. where an ion was ejected and recaptured by the same module demonstrating a recapture fidelity of 95.1% [32].

In this article, we show the demonstration of ion transport between two quantum computing modules at a transfer rate of 2424 s^{-1} with ion transfer fidelity of 99.999993%. Furthermore, we demonstrate that there is no measurable loss of coherence of the qubit during transport, therefore realising a high-fidelity coherent quantum matter-link between adjacent quantum computer modules.

II. EXPERIMENTAL SET-UP

We address the challenge of connecting independent QC modules by using two linear, segmented, surface-electrode Paul traps. Both ion-trap microchip modules have been fabricated such that the electrode structure extends to the edge of the inter-module gap. The chosen electrode structure allows for the confining potential from the electrodes to extend over the inter-module gap creating an electric field interface between the two modules.

One of the ion-trap modules ('Alice', left in Figure 3) is rigidly mounted to the vacuum chamber via a heatsink circulating cryogenic helium gas such that the trap operates at 36–42 K [33]. The second ion-trap module ('Bob', right in Figure 3) is cooled via a flexible copper braid forming a thermal link between the two modules. Bob is mounted to an in-vacuum three-axis piezo stage assembly that has a travel range of $600\text{ }\mu\text{m}$ and a positioning accuracy of 5 nm . However, since the measurement of the alignment of the two modules is done optically, the precision of the module alignment in the x - y plane is limited by the imaging system. To image the modules a lens system with $\times 13$ magnification is used in conjunction with an sCMOS camera. The imaging system has a spatial resolution of $0.5\text{ }\mu\text{m}$ which leads to an alignment error of $1\text{ }\mu\text{m}$ in the x - y plane. In the z -axis, the alignment is measured by scattering 369.5 nm of each of the modules' surfaces. The beam is aligned parallel to the plane of the modules and lowered onto either side of the inter-module gap. The difference in the beam height at which scatter is maximised on each of the modules is used to determine the alignment. This procedure leads to an alignment error in the z -axis of $3\text{ }\mu\text{m}$.

For results presented in this work the separation between Alice and Bob in each axis is $\Delta x = 10(1)\text{ }\mu\text{m}$, $\Delta y = 0(1)\text{ }\mu\text{m}$ and $\Delta z = 0(3)\text{ }\mu\text{m}$. From previous simulations [22], a misalignment in all three axes by $\leq 10\text{ }\mu\text{m}$ should lead to a RF barrier $\leq 0.2\text{ meV}$, which has been shown to be acceptable for high-fidelity ion transport [34].

$^{174}\text{Yb}^+$ and $^{171}\text{Yb}^+$ are used in this work. The qubit stored in $^{171}\text{Yb}^+$ is used to measure the effects of decoherence mechanisms on the matter-link, while $^{174}\text{Yb}^+$ is used for transfer fidelity measurements, due to its higher fluorescence rate.

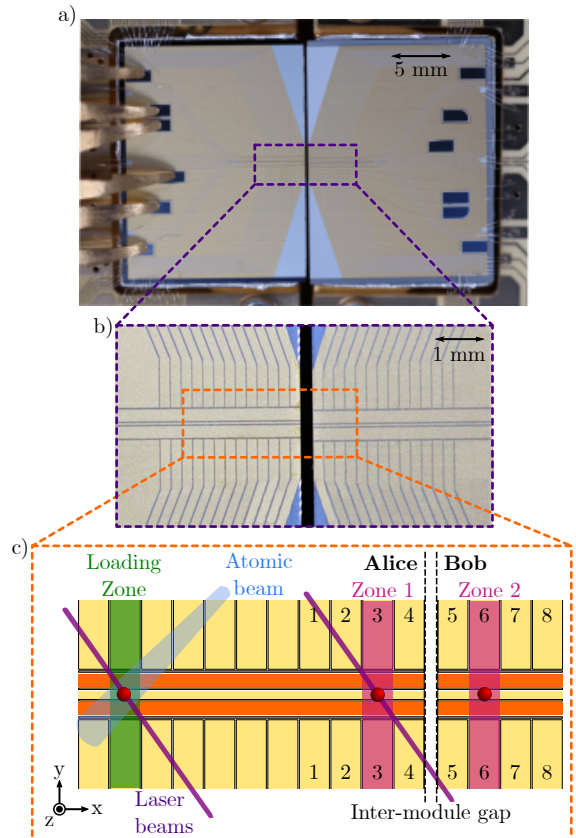


Figure 3. a) Picture of the two microfabricated ion-trap modules used to demonstrate inter-module transport. A dashed box overlay signifies the area depicted in b). b) Picture detailing the electrode structure of the two ion-trap modules. The image here has been modified to improve the clarity of the electrode structure. The dashed box overlay depicts the area represented in c). c) A schematic of 11 of the DC electrode pairs on the module Alice and 4 of the DC electrode pairs on the module Bob, electrodes pairs 1-8 are used for inter-module transport. The DC electrodes are in yellow and the RF electrodes are in orange. Ions are loaded into the trap in the Loading Zone with a restricted atomic beam and a set of laser beams. This prevents contamination of the electrodes around Zones 1 and 2. In the Loading Zone, 369.5 nm , 935.1 nm and 399.0 nm laser beams are overlapped. The 369.5 nm and 399.0 nm light is used for photo-ionisation, and the 369.5 nm and 935.1 nm light is used for Doppler cooling. Once an ion is loaded, the 399.0 nm light is turned off. Thereafter both the ion and the remaining laser beams are relocated to Zone 1. Detection of the ion occurs in Zone 1. Zone 1 and Zone 2 form the start and end points of an inter-module link.

To initialise the system, isotope selective loading occurs on Alice in the Loading Zone (Figure 3c). Once loaded, the ions are shuttled from the Loading Zone to Zone 1 over a distance of $1840\text{ }\mu\text{m}$, which is the starting point of all subsequent experiments. The details of the voltage control system can be found in Methods.

III. A QUANTUM MATTER-LINK

A. Inter-module Transport

Ion transport between modules is implemented by varying the voltages applied to the 4 electrode pairs closest to the inter-module gap on both Alice and Bob (1-8 in Figure 3c). Successive voltage updates sent to each electrode realise a translating potential well at the ion (see Methods). Each ion transfer Zone 1 \rightarrow Zone 2, or Zone 2 \rightarrow Zone 1 constitutes a single matter-link between modules. Zones 1 (2) were chosen as the start or end point of the link, since the ion can be confined independently on Alice (Bob) without requiring potentials from the neighbouring module. Zones 1 and 2 are separated by a distance of 684 μm . As an initial verification step, the success of the inter-module link was confirmed by imaging the scattered ion fluorescence in Zone 1 and in Zone 2, before and after ion transport. Thereafter, the lasers and detection optics were repositioned to detect ion fluorescence in Zone 1.

The inter-module transport fidelity was measured by moving $^{174}\text{Yb}^+$ between Zone 1 and Zone 2. After each set of 2×10^5 links the presence of the ion was verified by the detection of fluorescence using a photomultiplier tube (PMT). With a single link duration of 412.5 μs , at an equivalent link rate of 2424s^{-1} , 15×10^6 consecutive links were completed. The ion was lost during the following set of transport operations, indicating a lower limit of 99.999993% on the ion-transport fidelity. The ion travelled 10.26 km at an average transport speed of 1.66ms^{-1} . Throughout these transport measurements, the digital-to-analogue converters (DACs) were updated at the fastest possible rate. This led to distortions in the transport waveforms, resulting from the low cut-off frequency of the DC filtering circuits. No difference in the ion lifetime for stationary and shuttled ions was identifiable, therefore the transfer fidelity was not measurably affected by the distortions in the DC waveforms. The limit on the shuttling fidelity is therefore attributed to laser instability and ion loss from collisions with background gas molecules.

The limit on the speed of the shuttling was due to hardware constraints. Faster transport times can be achieved by changing to DACs with a faster update rate and by modifying the DC filter circuits to have a higher cut-off frequency (see Methods).

B. Preserving Qubit Coherence

To show that the coherence of the qubit can be maintained throughout the matter-link, the effect of the inter-module transport on qubit states is investigated. Here the qubit is formed using two hyperfine levels of $^{171}\text{Yb}^+$ in the $S_{1/2}$ manifold: $|0\rangle \equiv |F=0, m_f=0\rangle$, $|1\rangle \equiv |F=1, m_f=0\rangle$. The two states are separated by $12,642,812,118 + 311B^2$ Hz where B is the mag-

netic field in Gauss [10]. The ambient magnetic field at the qubit is approximately 10 G. The first order magnetic field insensitivity of the qubit (compared to the $|F=1, m_f=\pm 1\rangle$ states) increases its robustness against decoherence from ambient magnetic field fluctuations.

A Ramsey-type experiment is used to probe the coherence of the qubit by measuring the T_2^* time. This experiment is performed by first optically pumping the ion into the $|0\rangle$ state and subsequently applying two $\pi/2$ Ramsey pulses, separated by a delay time τ . The probability of the qubit being in $|1\rangle$ is then read out using a state-dependent fluorescence detection scheme [35]. The experiment is then repeated with inter-module transport operations taking place during the delay time τ (see Methods). Figure 4a shows an example of a stationary Ramsey experiment in comparison to results using 2 and 100 links within the delay time. The Ramsey fringe contrasts measured were 0.96(2), 1.00(2) and 0.97(2) for 0, 2 and 100 links respectively. The measured contrasts indicate that there is no measurable loss of qubit coherence during inter-module qubit transport for $\tau = 100$ ms.

Figure 4a shows phase offsets of 1.8690(1) rad and 3.7988(1) rad for the case for the 2 and 100 links respectively, relative to the stationary measurement. These phase offsets are attributed to uncompensated magnetic field drifts which occur over timescales longer than the experiment, along with a phase accumulation by the qubit which arises from its transport through magnetic field inhomogeneities. These phase offsets can be compensated for using an additional phase rotation after the transport operation.

Due to the limitations of the filter circuits and the DAC update rate (see Methods) shuttling techniques at diabatic timescales, where the motional state of the ion remains unchanged after transport, could not be used. Therefore, in order to limit the kinetic energy gain of the ion, which is required for optimal qubit state detection, an inter-module transfer rate of 1250s^{-1} was used.

Figure 4a demonstrates that, within the available measurement accuracy, qubit coherence is unaffected by inter-module transport at $\tau = 100$ ms. To investigate that qubit coherence is maintained throughout transport operations between QC modules more generally, the Ramsey-type experiment shown in Figure 4a was reproduced with longer delay times up to $\tau = 500$ ms. A Gaussian decay is then fitted to the fringe contrast to calculate a coherence time T_2^* . Figure 4b shows the coherence measurements and the resultant fits. For the stationary case, $T_2^* = 560(40)$ ms. With 2 links, $T_2^* = 560(60)$ ms, and with 100 links, $T_2^* = 540(30)$ ms. The main limiting factors of the coherence time are expected to be magnetic field fluctuations over the timescale of the experiment. Each of the 1-sigma errors of the measured coherence times overlap, demonstrating that we cannot detect a loss of coherence due to inter-module transport within the uncertainty of our measurement.

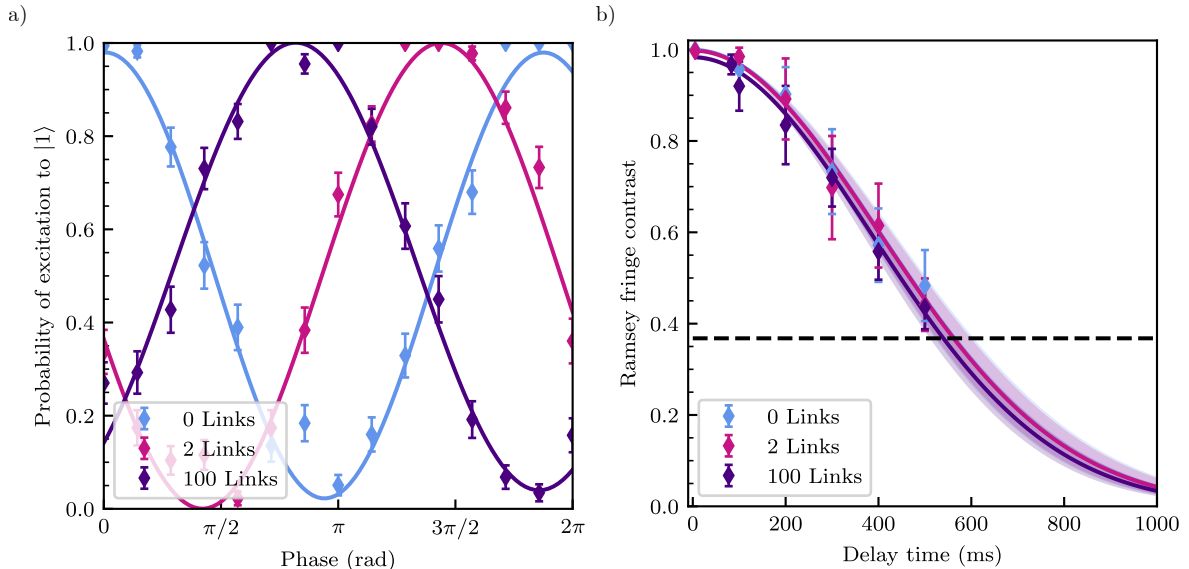


Figure 4. a) Ramsey fringes measured after 0, 2 and 100 links. The solid lines represent a sinusoidal fit to the data. For each dataset $\tau = 100$ ms, 100 averages were taken per data point. The Ramsey fringe contrasts are found to be 0.96(2), 1.00(2) and 0.97(2) for 0, 2 and 100 links respectively. b) The Ramsey fringe contrast as a function of time for 0, 2 and 100 links. The error bars represent the standard deviation in the measured contrast for a given time delay. The Gaussian fit to each dataset is given by the solid lines and the associated shaded areas represent the 1-sigma error in the fit. The dashed line indicates the $1/e$ decoherence threshold. The coherence times are 560(40) ms, 560(40) ms and 540(30) ms for 0, 2 and 100 links respectively.

IV. CONCLUSION

The techniques used in this work demonstrate that inter-module ion transport is a practical approach to interface QC modules. Two neighbouring microfabricated ion-trap modules were connected using ion transport operations, realising a fast, deterministic and high-fidelity quantum matter-link. This method of linking modules naturally extends the QCCD architecture from one to multiple modules. We therefore realise a key milestone towards the implementation of a scalable QCCD architecture. Furthermore, the inter-module link realised here is three orders of magnitude faster than the decoherence time. Future work will focus on increasing the connection rate using established ion transport techniques [36, 37]. This offers the potential of an additional order of magnitude increase in the inter-module shuttling rate.

METHODS

Effective connection rates for photonic interconnects

Scalable optical components are important for the implementation of a large-scale QC using photonic interconnects. To the best of the authors' knowledge, large switch arrays at trapped-ion wavelengths in the ultraviolet have yet to be developed. Alternatively, a large array of telecom wavelength switches combined with an ion-to-telecom wavelength conversion scheme could be used.

Telecom wavelength switches with low optical losses of 2.1 dB on average have been demonstrated [38]. Furthermore, conversions from Sr^+ or Yb^+ wavelengths to the telecom bands have been shown with conversion efficiencies of $\sim 9\%$ [39, 40]. Therefore, assuming a raw entanglement rate R , frequency up-conversion results in an up-converted rate of $0.09R$. Switch losses would then reduce this rate to $0.06R$. In addition, a distillation process may be required to achieve an entanglement fidelity within the fault-tolerant threshold. Using a 3 level distillation process as presented in Ref. [30] and as depicted in Figure 1a, a fidelity of 99.7% could be achieved from the current raw entanglement fidelity of 94%, at the cost of reducing the effective entanglement rate. Assuming all processes except the production of entangled pairs via remote entanglement are instantaneous and assuming a mixed-species gate can be achieved with 99.9% fidelity, the effective entanglement rate would be reduced by a factor of 6. This results in a distilled entanglement rate of $0.01R$. To complete the information transfer between two modules an additional set of gates is required as can be seen in Figure 1a. The time taken for this process is assumed to be instantaneous.

Ramsey experimental sequence

A schematic of the Ramsey-type experimental sequence can be seen in Figure 5, and can be broken down as follows: The ion is initially Doppler cooled for up

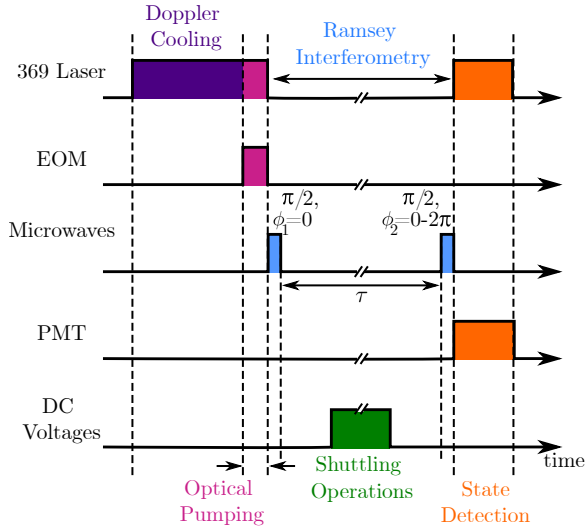


Figure 5. Pulse sequence diagram for the Ramsey-type experiment. The relative times of the different processes are represented on the same time axis (not to scale). From the top down the axes are: the on/off times for the 369.5 Doppler cooling laser, the electro-optic modulator (EOM) for optical pumping, the microwaves resonant with the qubit transition, the PMT for detection and the DC system for shuttling.

to 50 ms. Thereafter the ion is optically pumped into $|0\rangle$ over the course of $10\ \mu\text{s}$. The optical pumping is followed by an on-resonance microwave $\pi/2$ pulse with phase $\phi_1 = 0$ rad. The qubit is left to freely precess for a time delay τ , before a second $\pi/2$ pulse with phase offset of $0 \leq \phi_2 \leq 2\pi$ rad is applied. For each phase offset, the measurement is repeated 100 times. To measure the coherence time, the experimental sequence was repeated for $\tau = \{5, 100, 200, 300, 400, 500\}$ ms for the stationary and 2 link data whereas the 100 link data spanned $\tau = \{83, 100, 200, 300, 400, 500\}$ ms. When investigating the impact of the matter-link on the T_2^* time, a variable number $N = \{2, 100\}$ of qubit transport operations can be undertaken within the delay time τ , such that $NT_L < \tau$, where T_L is the time taken for one link.

DC ion transfer protocol

A Sinara Kasli field-programmable gate array (FPGA) controller equipped with three AD5432 digital-to-analog converter (DAC) Zotino cards is used to control the DC waveforms applied to the ion-trap modules, for ion transport. The DAC cards update at a rate of 139 kHz per channel. Each DAC channel has an internal third-order Butterworth filter with 75 kHz cut-off frequency. In addition, a second set of second-order RC filters with a 47 kHz cut-off frequency is used prior to the vacuum chamber. Inside the vacuum chamber each DC channel is connected to a final first-order RC filter with a 257 kHz cut-off frequency. The axial trap frequency is $\nu_{ax} = \omega_{ax}/2\pi = 141(1)$ kHz and the radial frequencies

are $\nu_{rad} = \omega_{rad}/2\pi = 1.15(3)$ and $1.31(3)$ MHz.

The ion transfer waveforms are numerically determined from a Finite Element Method (FEM) electrostatic simulation. The simulation includes electrode potentials for both ion-trap modules. In order to calculate the potentials, a sequential least-squares programming (SLSQP) optimiser is used to minimise a cost function for a given ion position. The cost function is constructed to fulfil the following criteria:

- Minimise the electric field at the ion position.
- Constrain the axial electric field curvature, and thus the axial secular frequency, to a predetermined value.
- Minimise the sum of the squares of the voltage across all electrodes.

Using this method, a set of voltage values is calculated. For the simulations used in this work, potentials were calculated in $2\ \mu\text{m}$ steps between Zones 1 and 2. This provides trapping potentials that are linearly incremented along the ion transport path. The evolution of the voltage on each electrode is further post-processed using a second-order Savitzky–Golay filter [41] with a moving filter window of 25 voltage values. This post-processing removes numerical noise resulting from non-optimal minimisations of the cost function, without distorting the waveform.

From the post-processed waveforms, the sets of voltage solutions were down-sampled to provide $12\ \mu\text{m}$ incremented solutions for ion transport. This axial separation between steady state potential minima in the shuttling sequence was found to provide the best trade-off between shuttling rate and shuttling fidelity.

ACKNOWLEDGEMENTS

The authors thank David Breaud for providing valuable technical assistance with the DC filtering system and Christophe Valahu for helpful discussions with the planning of the Ramsey experiment. Ion-trap module microfabrication was carried out at a number of facilities including the Center of MicroNanoTechnology (CMi) at the École Polytechnique Fédérale de Lausanne (EPFL), the London Centre for Nanotechnology (LCN), and the Scottish Microelectronics Centre (SMC) at the University of Edinburgh. This work was supported by the U.K. Engineering and Physical Sciences Research Council via the EPSRC Hub in Quantum Computing and Simulation (EP/T001062/1), the U.K. Quantum Technology hub for Networked Quantum Information Technologies (No. EP/M013243/1), the European Commission's Horizon-2020 Flagship on Quantum Technologies Project No. 820314 (MicroQC), the U.S. Army Research Office under Contract No. W911NF-14-2-0106 and Contract No. W911NF-21-1-0240, the Office of Naval Re-

search under Agreement No. N62909-19-1-2116, the Luxembourg National Research Fund (FNR) (Project Code 11615035), the University of Sussex, the Engineering and Physical Sciences Research Council (EP/SO23607/1,

EP/SO21582/1) via the Quantum Engineering Centre for Doctoral Training at the University of Bristol & the Centre for Doctoral Training at the University College London.

-
- [1] Hucul, D. *et al.* Modular entanglement of atomic qubits using photons and phonons. *Nature Physics* **11**, 37–42 (2015).
- [2] Kurpiers, P. *et al.* Deterministic quantum state transfer and remote entanglement using microwave photons. *Nature* **558**, 264–267 (2018).
- [3] Magnard, P. *et al.* Microwave quantum link between superconducting circuits housed in spatially separated cryogenic systems. *Physical Review Letters* **125**, 260502 (2020).
- [4] Stephenson, L. J. *et al.* High-rate, high-fidelity entanglement of qubits across an elementary quantum network. *Phys. Rev. Lett.* **124**, 110501 (2020).
- [5] Gold, A. *et al.* Entanglement across separate silicon dies in a modular superconducting qubit device. *npj Quantum Information* **7**, 1–10 (2021).
- [6] Pompili, M. *et al.* Realization of a Multinode Quantum Network of Remote Solid-State Qubits. *Science* **372**, 259–264 (2021).
- [7] Wineland, D. J. *et al.* Experimental issues in coherent quantum-state manipulation of trapped atomic ions. *Journal of Research of the National Institute of Standards and Technology* **103**, 259 (1998).
- [8] Kielpinski, D., Monroe, C. & Wineland, D. J. Architecture for a large-scale ion-trap quantum computer. *Nature* **417**, 709–711 (2002).
- [9] Bruzewicz, C. D., Chiaverini, J., McConnell, R. & Sage, J. M. Trapped-ion quantum computing: Progress and challenges. *Applied Physics Reviews* **6** (2019).
- [10] Wang, P. *et al.* Single ion qubit with estimated coherence time exceeding one hour. *Nature Communications* **12**, 233 (2021).
- [11] Harty, T. P. *et al.* High-fidelity preparation, gates, memory, and readout of a trapped-ion quantum bit. *Phys. Rev. Lett.* **113**, 220501 (2014).
- [12] Srinivas, R. *et al.* High-fidelity laser-free universal control of trapped ion qubits. *Nature* **597**, 209–214 (2021).
- [13] Monz, T. *et al.* 14-Qubit entanglement: creation and coherence. *Physical Review Letters* **106**, 130506 (2011).
- [14] Ladd, T. D. *et al.* Quantum computers. *Nature* **464**, 45–53 (2010).
- [15] Popkin, G. Quest for qubits. *Science* **354**, 1090–1093 (2016).
- [16] Wright, K. *et al.* Benchmarking an 11-qubit quantum computer. *Nature Communications* **10**, 1–6 (2019).
- [17] Pogorelov, I. *et al.* Compact ion-trap quantum computing demonstrator. *PRX Quantum* **2**, 1 (2021).
- [18] Pino, J. M. *et al.* Demonstration of the trapped-ion quantum CCD computer architecture. *Nature* **592**, 209–213 (2021).
- [19] Egan, L. *et al.* Fault-tolerant control of an error-corrected qubit. *Nature* **598**, 281–286 (2021).
- [20] Brown, K. R., Kim, J. & Monroe, C. Co-designing a scalable quantum computer with trapped atomic ions. *npj Quantum Information* **2**, 16034 (2016).
- [21] Kaufmann, P., Gloger, T. F., Kaufmann, D., Johanning, M. & Wunderlich, C. High-fidelity preservation of quantum information during trapped-ion transport. *Physical Review Letters* **120**, 010501 (2018).
- [22] Lekitsch, B. *et al.* Blueprint for a microwave trapped ion quantum computer. *Science Advances* **3**, 1–12 (2017).
- [23] Ryan-Anderson, C. *et al.* Realization of real-time fault-tolerant quantum error correction. *Physical Review X* **11**, 41058 (2021).
- [24] Hilder, J. *et al.* Fault-tolerant parity readout on a shuttling-based trapped-ion quantum computer. *Physical Review X* **12**, 011032 (2022).
- [25] Gidney, C. & Ekerå, M. How to factor 2048 bit RSA integers in 8 hours using 20 million noisy qubits. *Quantum* **5**, 1–31 (2021).
- [26] Webber, M., Elfving, V., Weidt, S. & Hensinger, W. K. The impact of hardware specifications on reaching quantum advantage in the fault tolerant regime. *AVS Quantum Science* **4**, 013801 (2021).
- [27] Lee, J. *et al.* Even more efficient quantum computations of chemistry through tensor hypercontraction. *PRX Quantum* **2**, 1 (2021).
- [28] Monroe, C. & Kim, J. Scaling the ion trap quantum processor. *Science* **339**, 1164–1169 (2013).
- [29] Monroe, C. *et al.* Large-scale modular quantum-computer architecture with atomic memory and photonic interconnects. *Physical Review A* **89**, 022317 (2014).
- [30] Nigmatullin, R., Ballance, C. J., de Beaudrap, N. & Benjamin, S. C. Minimally complex ion traps as modules for quantum communication and computing. *New Journal of Physics* **18** (2016).
- [31] Awschalom, D. *et al.* Development of quantum interconnects (QuICs) for next-generation information technologies. *PRX Quantum* **2**, 1–21 (2021).
- [32] Stopp, F., Lehec, H. & Schmidt-Kaler, F. A deterministic single ion fountain (2021). URL <https://arxiv.org/abs/2108.06948v1><http://arxiv.org/abs/2108.06948>. 2108.06948.
- [33] Lebrun-Gallagher, F. R. *et al.* A scalable helium gas cooling system for trapped-ion applications. *Quantum Science and Technology* (2022). URL <https://doi.org/10.1088/2058-9565/ac5d7d>.
- [34] Blakestad, R. B. *et al.* High-fidelity transport of trapped-ion qubits through an X-junction trap array. *Physical Review Letters* **102**, 1–4 (2009).
- [35] Olmschenk, S. *et al.* Manipulation and detection of a trapped Yb⁺ hyperfine qubit. *Physical Review A* **76**, 052314 (2007).
- [36] Bowler, R. *et al.* Coherent diabatic ion transport and separation in a multizone trap array. *Physical review letters* **109**, 080502 (2012).
- [37] Walther, A. *et al.* Controlling fast transport of cold trapped ions. *Physical review letters* **109**, 080501 (2012).
- [38] Kim, J. *et al.* 1100 × 1100 port MEMS-based optical crossconnect with 4-dB maximum loss. *IEEE Photonics*

- Technology Letters* **15**, 1537–1539 (2003).
- [39] Kasture, S. *et al.* Frequency conversion between UV and telecom wavelengths in a lithium niobate waveguide for quantum communication with Yb⁺ trapped ions. *Journal of Optics* **18** (2016).
- [40] Wright, T. A. *et al.* Two-way photonic interface for linking the Sr⁺ transition at 422 nm to the telecommunication C band. *Physical Review Applied* **10**, 1 (2018).
- [41] Savitzky, A. & Golay, M. J. Smoothing and differentiation of data by simplified least squares procedures. *Analytical chemistry* **36**, 1627–1639 (1964).